Temporal complexity of fMRI is reproducible and correlates with higher order cognition

Amir Omidvarnia[1,2], Andrew Zalesky[3,4], Dimitri Van De Ville[5,6],
Graeme D. Jackson[1,2,7], and Mangor Pedersen[1,2]

[1] *The Florey Institute of Neuroscience and Mental Health, Melbourne Brain Centre, Australia*
[2] *Florey Department of Neuroscience and Mental Health, The University of Melbourne, Australia*
[3] *Melbourne Neuropsychiatry Centre, Department of Psychiatry, The University of Melbourne, Australia*
[4] *Department of Biomedical Engineering, The University of Melbourne, Australia*
[5] *Institute of Bioengineering, Center for Neuroprosthetics, Center for Biomedical Imaging, EPFL, Lausanne, Switzerland*
[6] *Department of Radiology and Medical Informatics, University of Geneva, Geneva, Switzerland*
[7] *Department of Neurology, Austin Health, Melbourne, Australia*

Abstract

In 2014, McDonough and Nashiro [1] derived multiscale entropy –a marker of signal complexity– from resting state functional MRI data (rsfMRI), and found that functional brain networks displayed unique multiscale entropy fingerprints. This is a finding with potential impact as an imaging-based marker of normal brain function, as well as pathological brain dysfunction. Nevertheless, a limitation of this study was that rsfMRI data from only 20 healthy individuals was used for analysis. To overcome this limitation, we aimed to replicate McDonough and Nashiro's finding in a large cohort of healthy subjects. We used rsfMRI from the Human Connectome Project (HCP) comprising 936 gender-matched healthy young adults aged 22-35, each with 4×14.4-minute rsfMRI data from 100 brain regions. We quantified multiscale entropy of rsfMRI time series averaged at different cortical and sub-cortical regions. We also performed a test-retest analysis on the data of four recording sessions in 10 previously reported resting state networks (RSNs). Given that the morphology of multiscale entropy patterns is affected by the choice of the tolerance parameter (r), we performed the analyses at two r values: 0.5, similar to the original study and 0.15, a commonly used option in the literature. Our results were similar to previous findings by McDonough and Nashiro emphasising high temporal complexity in the default mode network and fronto-parietal networks, and low temporal complexity in the cerebellum. We also investigated the effect of temporal resolution (determined by fMRI repetition time) by downsampling rsfMRI time series. At a low temporal resolution, we observed increased entropy and variance across datasets likely due to fewer data points in the multiscale entropy analysis. Test-retest analysis showed that findings were likely reproducible across individuals over four rsfMRI runs, especially for $r = 0.5$. We also showed a positive relationship between temporal complexity of RSNs and fluid intelligence (people's capacity to reason and think flexibly), suggesting that complex dynamics is an important attribute of optimized brain function.

Key words: complexity, entropy, multiscale entropy, fMRI, HCP, human connectome project, behaviour, fluid intelligence, reproducibility, resting state network

1   Introduction

The human brain is a complex hierarchy of modules that are dynamically interacting with each other at micro, meso and macro scales [2, 3]. Anatomically distinct regions of the cortex that simultaneously fluctuate over time are referred to as functionally connected *resting state networks* (*RSNs*). RSNs are interinsic organizations of functional connectivity in the brain that are communicating with each other even in the absence of an overt cognitive tasks [4–6]. These brain networks can be derived from resting state functional magnetic resonance imaging (rsfMRI), and are supporting a variety of sensory, cognitive and behavioural functions [7, 8]. Perturbed functionality of RSNs contributes to a range of brain diseases including epilepsy [9], Alzheimer's disease [10], autism [11], depression [12] and schizophrenia [13]. Although alterations of RSNs have been subject to numerous studies, characterization of their complex dynamics remains an open question in the brain sciences [1, 14–21]. This is a significant challenge in modern neuroscience because temporal brain complexity may provide a quantitative view of brain function at the phenomenological level which in turn, may leads to the development of more efficient diagnostic and prognostic markers of brain diseases.

Functional co-activations associated with RSNs fluctuate over time [22, 23]. Until recently, most studies would treat brain functional connectivity as a *static* entity. The emergence of advanced neuroimaging techniques such as fast rsfMRI have opened up a new avenue for studying the dynamics of functional connectivity [24]. There is now a consensus that this dynamic behaviour is temporally complex, meaning that it resides between temporal order (regularity) and disorder (randomness) [25–27]. Temporal complexity of brain dynamics arises from interactions across numerous sub-components in the brain [1] and can be affected by internal and/or external factors such as sensory inputs, attention and drowsiness [28]. Examples include self-similarity of EEG microstate sequences [29, 30], dynamics of microscopic and mesoscopic neural networks in the brain [3, 31] and neuronal oscillations associated with different brain regions [32]. Several attempts have been made to characterize the temporal complexity of RSNs using rsfMRI data including, but not limited to, time-frequency analysis [23], independent components analysis [33], point process analysis [34], sliding window analysis [35], phase synchrony analysis [36, 37], autoregressive modelling [38] and nonlinear analysis [1, 18, 39, 40] (see [24] for a detailed review). These studies have a common purpose, namely to characterize complex behaviour of brain functional oscilations. An important form of complexity in brain function is observed in the dynamics of RSNs, as shown by McDonough and Nashiro, is *multiscale entropy* [1]. Multiscale entropy [41, 42] quantifies the rate of generation of new information in a dynamic process. This is achieved by computing sample entropy [43] over multiple temporal scales. Each scale provides a specific time resolution through coarse graining of the input signals. For example, random signals such as white noise have high sample entropy values at fine scales (i.e., fast fluctuations) which drop gradually in value at large scales (i.e., slow fluctuations). On the other hand, complex signals such as random walk or biosignals generate a more consistent sample entropy curve over different time scales, due to repeating information-bearing patterns across multiple time resolutions [20, 41, 42, 44].

In this paper, we hypothesized that RSNs can be differenciated by their complex dynamics. To this end, we aimed to replicate a particular study by McDonough and Nashiro published in 2014 [1] hypothesizing the existence of temporally complex fingerprints in rsfMRI RSNs. These authors used rsfMRI datasets of 20 healthy subjects from the Human Connectome Project (HCP) [45] and analysed multiscale entropy [41] within four RSNs: default mode network, central executive network, as well as the left and right frontotemporal networks (Figure 1). Given that signal complexity of RSNs may be an imaging-based marker of brain functional networks in health and disease, we aimed to investigate this hypothesis in a larger sample cohort of 936 gender-matched rsfMRI datasets from the HCP database. In contrast to [1], we included an additional six RSNs in this study, with a particular focus to what extent rsfMRI results are dependent on the tolerance parameter r in multiscale entropy. We also conduced a test-retest analysis to delineate the reproducibility of multiscale entropy patterns across multiple rsfMRI scans and after downsampling. Lastly, we hypothesized that brain complexity is related to higher order cognitive processes including working memory, intelligence and cognitive flexibility.

Original finding by McDonough and Nashiro (2014) in 20 subjects
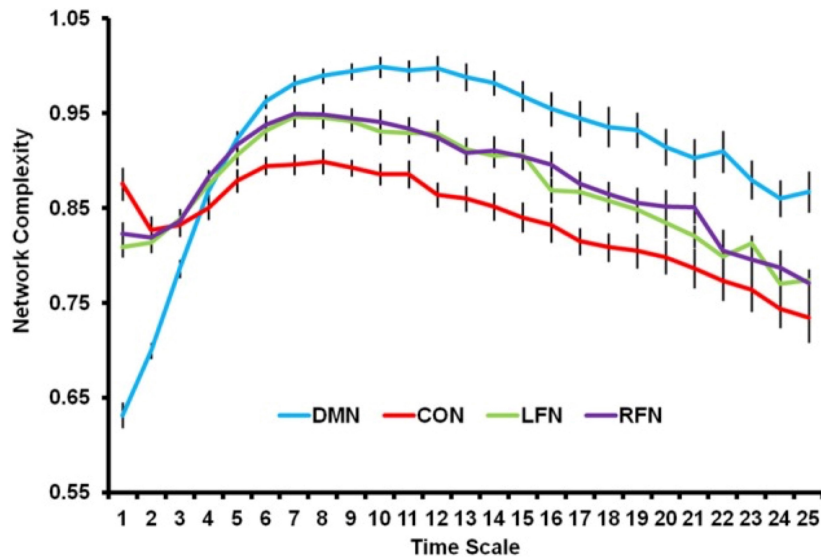
Figure 1: Original finding by McDonough and Nashiro [1]: rsfMRI-extracted RSNs (i.e., default mode network, central executive network or CON, left frontal network or LFN, right frontal network or RFN) show characteristic multiscale entropy patterns. The image is reproduced from [1].

2 Materials and Methods

2.1 rsfMRI Data, parcellation masks and preprocessing

We used an equi-gender subset of the HCP database [45] including 936 rsfMRI datasets from a population of 1003 subjects (N_{subj}=936). Each subject underwent four rsfMRI runs of length 14.4 minutes (or 1200 time points) with a voxel size of $2\times2\times2$ millimeters the repetition time (T_R) of 720 milliseconds in a 3T scanner. The following minimal preprocessing steps were applied on the data of each subject from the HCP database: 1) echo planar imaging gradient distortion correction, 2) motion correction, 3) field bias correction, 4) spatial transformation, 5) normalization into a common Montreal Neurological Institute space [46] and 6) artefact removal using independent component analysis FIX [47]. Another independent components analysis was applied at the group level of 1003 subjects to obtain a brain parcellation mask with 100 regions of interests (N_{ROI}=100) covering the entire brain including 55 sub-cortical and 45 cortical parcels. The datasets are publicly available at the HCP website under an Open Access Data plan agreement.

2.2 From brain regions to RSNs

Figure 2 illustrates the multiscale entropy analysis approach that we applied on the HCP datasets. We obtained binarized masks of RSNs by thresholding normalized templates provided by Smith *et al* in [48], at *Z*-score=3. We analysed 10 networks as follows: default mode network, primary and secondary visual networks, cerebellum, sensorimotor network, auditory network, executive control network as well as left and right frontoparietal networks (Figure 1 in [48] - also reproduced in Figure S1).

In order to match between 100 parcellated brain regions in the rsfMRI datasets and 10 RSNs, we grouped multiscale entropy curves of brain regions that spatially overlapped with the same RSNs (see the binary adjacency matrix between brain regions and networks in Figure 2). Since brain regions of interest were associated with non-binarized independent component maps in the HCP database, we assigned each region to a specific RSN if the maximum voxel of its associated independent component map was within the spatial extent of the given network. This procedure reduced the number of brain regions from 100 to 64 for analysis, because some sub-cortical regions did not spatially overlap with any of the RSNs. For each dataset, we extracted multiscale entropy curves of mean rsfMRI time series

3

associated with 64 parcellated brain regions over 25 time scales resulting in a subject-specific multiscale entropy matrix of size 64×25.

Block diagram of the analysis pipeline
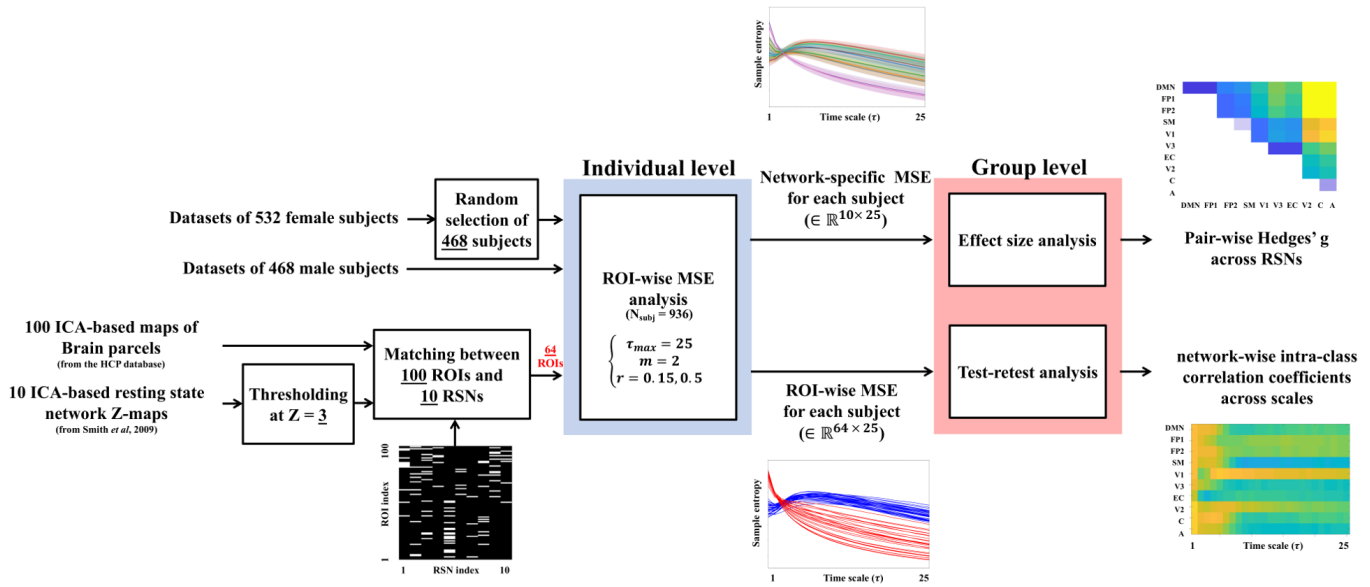
Figure 2: Analysis pipeline of the current study at the individual and group levels. Multiscale entropy curves on the top are examples over 10 RSNs, while the curves at the bottom exemplify 64 brain regions of interest (blue for cortical regions and red for sub-cortical regions). See sections 2.3.1 and 2.3.2 for more details. The binary adjacency matrix shows the pair-wise overlaps between 100 brain regions and 10 RSNs. The effect size and test-retest analyses are explained in sections 2.3.5 and 2.3.6, respectively. **Abbreviation**: MSE = multiscale entropy, RSN = resting state network, ROI = (brain) region of interest, ICA = independent components analysis.

2.3 Signal entropy analysis

While there are several definitions of signal entropy in the literature, our focus here is on multiscale entropy analysis [41, 42]. This technique is an extended version of the sample entropy measure over multiple time scales.

2.3.1 Sample entropy

Sample entropy [43] is a signal complexity measure which treats each short piece of an input signal $\mathbf{x}$ as a *template* to search for any *neighbouring* templates throughout its entire length of the signal. A template $\mathbf{X}_i^m$ is defined as[1]:

$$\mathbf{X}_i^m = \{x_i, \ x_{i+1}, \ ... \ , \ x_{i+m-1}\}, \ i = 1, ..., N - m + 1. \tag{1}$$

where N is the number of time points in $\mathbf{x}$ and m is the embedding dimension parameter. Two templates $\mathbf{X}_i^m$ and $\mathbf{X}_j^m$ are considered as neighbours if their Chebyshev distance $d(\mathbf{X}_i^m, \mathbf{X}_j^m)$ is less than a *tolerance* parameter r. It leads to an r-neighbourhood conditional probability function $C_i^m(r)$ for any vector $\mathbf{X}_i^m$ in the m-dimensional reconstructed phase space:

$$C_i^m(r) = \frac{1}{N - m + 1} B_i^m(r), \ i = 1, ..., N - m + 1, \tag{2}$$

where $B_i^m(r)$ is given by:

$$B_i^m(r) = \sum_{j=1}^{N-m} \Psi(r - d(\mathbf{X}_i^m, \mathbf{X}_j^m)), \tag{3}$$

---

[1]In all equations, scalar variables are in normal font, while vector variables are in bold.

where $\Psi(.)$ is the Heaviside function, defined as:

$$\Psi(a) = \begin{cases} 0 & a < 0 \\ 1 & a \geq 0. \end{cases} \tag{4}$$

The Chebyshev distance d is defined as:

$$d(\mathbf{X}_i^m, \mathbf{X}_j^m) := \max_k(|x_{i+k} - x_{j+k}|, \ k = 0, ..., m-1). \tag{5}$$

Sample entropy is then given by:

$$SampEn_\tau(m, r) = \lim_{N \to \infty} -ln \, \frac{\mathcal{B}_{m+1}^r}{\mathcal{B}_m^r}, \tag{6}$$

where $\mathcal{B}_m^r$ is the average of $B_i^m(r)$'s over all templates:

$$\mathcal{B}_m^r = \frac{1}{N-m} \sum_{i=1}^{N-m} B_i^m(r). \tag{7}$$

Since $d(\mathbf{X}_i^m, \mathbf{X}_j^m)$ is always smaller than or equal to $d(\mathbf{X}_i^{m+1}, \mathbf{X}_j^{m+1})$, $\mathcal{B}_{m+1}^r$ will always take smaller or equal values than $\mathcal{B}_m^r$. Therefore, sample entropy is always non-negative with larger values indicating less regularity [43]. The tolerance parameter r plays a central role in any sample entropy analysis, because it defines the probability of neighbourhood (i.e., similarity) between two templates in the reconstructed phase space. It is important to multiply r by the standard deviation of $\mathbf{x}$ to account for amplitude variations across different signals [18, 43]. In this study, we used the embedding dimension of $m=2$ and the tolerance parameter of $r=0.15$ for sample entropy analysis, as widely used options in the literature (see [49, 50] ans examples). In addition, we used the tolerance parameter of $r=0.5$, as adapted by McDonough and Nashiro [1].

2.3.2 Multiscale entropy

Multiscale entropy extracts sample entropy after *coarse-graining* of the input signal $\mathbf{x}$ at a range of time scales τ [41]. A coarse-grained vector $\mathbf{x}(\tau) = \{x_i(\tau)\}$ is defined as:

$$x_i(\tau) = \frac{1}{\tau} \sum_{k=(i-1)\tau+1}^{i\tau} x_k, \quad \tau = 1, 2, ..., \tau_{max}. \tag{8}$$

Following the study of [1], we set τ_{max} to 25. At the group level, we averaged the multiscale entropy curves over subjects and calculated the standard deviation at each scale. We also computed the complexity index (i.e., area under the curve) of multiscale entropy patterns for each network, in all datasets.

2.3.3 Complexity index

To reduce the dimensionality of multiscale entropy patterns to a single value, a complexity index is defined as the area under each multiscale entropy curve over all scales, divided by the maximum number of scales (i.e., τ_{max}) [51]. For a single subject, it can be approximated by averaging of sample entropy values across multiple time scales (up to τ_{max}):

$$M_i = \frac{1}{\tau_{max}} \sum_{\tau=1}^{\tau_{max}} SampEn_\tau(m, r). \tag{9}$$

2.3.4 The role of rsfMRI temporal resolution

Given the relatively short repetition time of rsfMRI time series in the HCP database (T_R=0.72 seconds), we investigated to what extent the observed complex dynamics of RSNs is sensitive to rsfMRI temporal resolution. This is an important issue to check, because T_R values longer than one second are common across research and clinical centres. We resembled longer T_R's in our datasets by downsampling of the rsfMRI time series in the HCP database. To this end, we calculated the complexity indices of RSNs after downsampling of the rsfMRI time series at the rates of 2 and 4, resembling the repetition times of T_R=1.44 seconds and T_R=2.88 seconds, respectively.

Multiscale entropy analysis of color noise
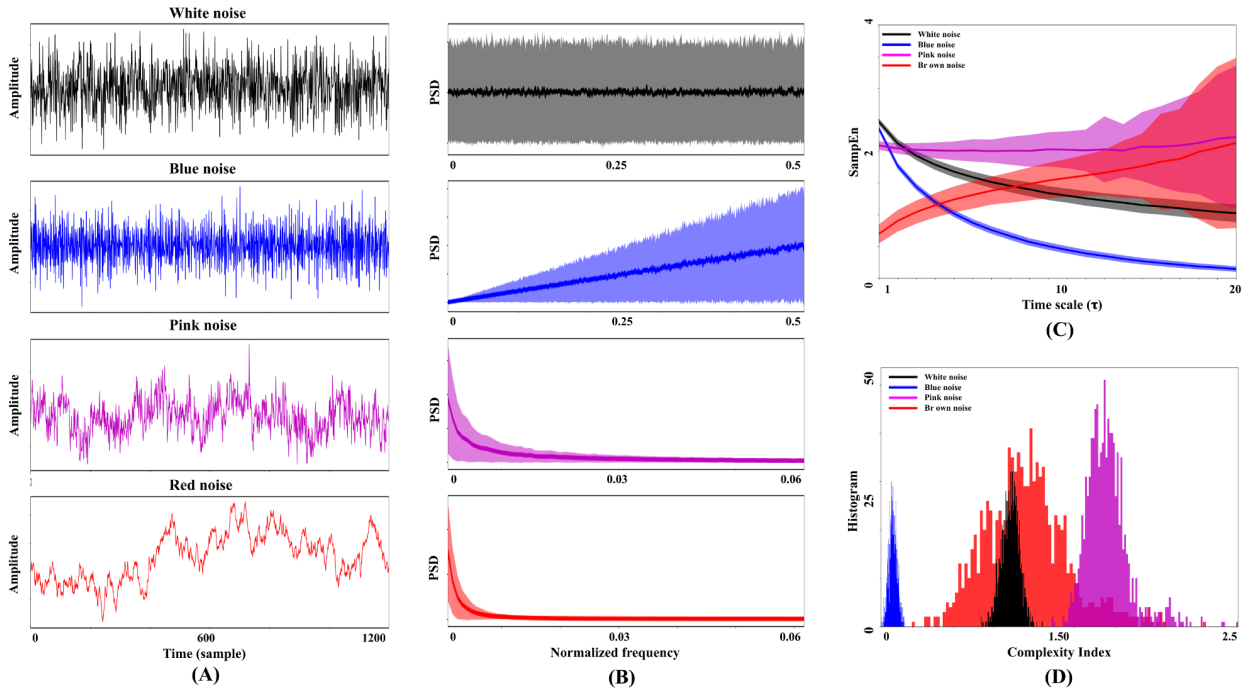
Figure 3: Multiscale entropy of white noise in black color, blue noise in blue color, pink noise in pink color and red (Brown) noise in red color (m=2, r=0.15). For each noise type, 100 random realizations were generated. Column (A) Exemplary realizations in the time domain. Column (B) Shaded error bars of power spectral density functions associated with 100 realizations. (C) Distributions of multiscale entropy patterns over 100 realizations. Shaded regions show one standard deviation from the mean curve. (D) Distributions of complexity index values.

2.3.5 Effect size analysis using the Hedges' g measure

We quantified the difference between complex dynamics of RSNs by pair-wise effect size analysis of the complexity index distributions at three temporal resolutions (i.e., original T_R of 0.72 seconds and two downsampling rates) as well as two choices of the tolerance parameter (i.e., r=0.15, 0.5). To this end, we used the Hedges' $g_{i,j}$ statistic, defined as [52]:

$$g_{i,j} = \frac{M_i - M_j}{\sigma^*_{i,j}}, \tag{10}$$

where M_i and M_j are the group mean complexity indices of the ith and j^{th} RSNs, respectively, and $\sigma^*_{i,j}$ is the squared mean of the associated standard deviations computed as:

$$\sigma^*_{i,j} = \sqrt{\frac{\sigma_i^2 + \sigma_j^2}{2}}. \tag{11}$$

For the HCP datasets, the confidence interval and p-value of the Hedges' g measures were calculated through bootstrapping (2000 random samplings of the original time series with replacement)[2]. For the

---

[2]The effect size analysis toolbox associated with [53] is available at the MATLAB File Exchange website.

epilepsy study, however, we used an exact analytical computation of the confidence intervals, given its low sample size. See [53] for more details.

2.3.6 Test-retest analysis using the intra-class correlation coefficient

In order to investigate the reproducibility of multiscale entropy patterns extracted from RSNs at different temporal resolutions, we computed intra-class correlation coefficient of sample entropy values at single time scales and over rsfMRI scans (N_{run}=4). Following [54], we chose the third intra-class correlation coefficient measure defined in [55] for test-retest analysis as:

$$ICC_i(\tau) = \frac{BMS_i(\tau) - EMS_i(\tau)}{BMS_i(\tau) + (N_{run} - 1)EMS_i(\tau)}, \tag{12}$$

where $BMS_i(\tau)$ and $EMS_i(\tau)$ are the *between-subjects mean square* and the *error mean square* of sample entropy values, respectively, for the ith RSN at the time scale τ. We considered the intra-class correlation coefficient values below 0.4 as poor reliability, between 0.4 and 0.6 as fair reliability and between 0.6 and 0.8 as good reliability [54].

2.4 Temporal complexity of RSNs and cognition

We also tested whether temporal complexity of fMRI is related to higher order cognition. For each subject ($N_{subj} = 936$), we selected five well-validated domain-specific behavioural variables ($N_{beh} = 5$) involved in higher order cognition; *i*) the Eriksen flanker task (*Flanker_ Unadj* — measuring response inhibition and task switching); *ii*) the Wisconsin Card Sorting Test (*CardSort_ Unadj* — measuring cognitive flexibility); *iii*) the N-back task (*WM_ Task_ acc* — measuring working memory performance); *iv*) the Ravens task (*PMAT24_ A_ CR* — measuring fluid intelligence); and *v*) the relational task (*Relational_ Task_ Acc* — measuring planning and reasoning abilities). See also [56], for full information about behavioural variables included in the HCP. We defined a multiple linear regression model with N_{beh} independent variables as follows:

$$\hat{\mathbf{M}}_i = \hat{\beta}_i(0) + \hat{\beta}_i(1)\mathbf{b}_1 + ... + \hat{\beta}_i(N_{beh})\mathbf{b}_{N_{beh}}, \tag{13}$$

where $\hat{\mathbf{M}}_i \in \mathbb{R}^{N_{subj} \times 1}$ is the predicted vector of subject-specific complexity indices in the ith RSN and $\mathbf{b}_k \in \mathbb{R}^{N_{subj} \times 1}$ is the associated vector of kth behavioural measures ($k = 1, ..., N_{beh}$). For each estimated $\hat{\beta}_i(k)$, we performed a t-test at the 5% significance level whether the coefficient is equal to zero or not. To assess whether the correlation coefficients between real complexity indices $\mathbf{M}_i$ and their predicted associates $\hat{\mathbf{M}}_i$ are statistically significant, we performed a permutation testing for each RSN where we permuted the order of subjects in $\mathbf{M}_i$, refitted the model and repeated this procedure for 10000 times. It led to an empirical null distribution for each network.

To assess the contribution of each behavioural variable into the temporal complexity of RSNs, we performed a bidirectional step-wise regression analysis where the independent variables were added or removed based on their importance to the fitted model in an iterative fashion [57]. The procedure continues until no further improvement can be obtained in the goodness of fit of the regression model (here, at a significance level of p<0.05).

3 Results

3.1 Simulation: Multiscale entropy analysis of color noise

To demonstrate the capacity of multiscale entropy analysis for encoding signal dynamics, we simulated 100 realizations of four color noise signals (white, blue, pink and red) with 1200 time-points and computed their multiscale entropy patterns (m=2, r=0.15). See Figure 3-A, B for exemplary realizations of the noise types and their associated power spectral densities. As Figure 3-C shows, multiscale entropy

curves of each noise type are distinct and can be considered as their dynamical signature. The associated complexity index values are also an informative indicator of the time-varying nature in each noise type, except for white and red noise whose complexity distributions fully overlap (Figure 3-D). Among the four, blue and white noises lead to lower complexity indices, while pink and red noises resemble complex signals due to their $1/f^\beta$ spectral density functionas and fractal properties [58].

3.2 RSNs are temporally complex

We observed distinct multiscale entropy patterns between cortical and sub-cortical parts of RSNs (64 regions in total illustrated as blue and red curves in Figure 4 - see also Figure 2 for the procedure of defining cortical and sub-cortical regions). A visual comparison between cortical/sub-cortical multiscale entropy curves (Figure 4-A) and simulated noise processes (Figure 3-C) suggests that the entropy patterns of cortical regions are closer to the morphology of synthetic complex signals such as pink noise and red noise, while sub-cortical brain regions are more similar to non-complex, and random, signals such as white noise and blue noise. This observation was the same for both values of the tolerance parameter r (Figure 4- panel A versus panel B).

Our multiscale entropy analysis of RSNs at r=0.5 led to near-identical entropy patterns to the original study by McDonough and Nashiro [1] where the default mode network, left and right frontoparietal networks and central executive network were studied (our replication is displayed in Figure 4-D; the original finding is displayed in Figure 1 – both with the parameters m=2, r = 0.5 and time scales from 1 to 25). It is worth noting that both the original study [1] and our study used similar spatial templates of RSNs provided in [48] - see Figure S1. Similar to [1], the multiscale entropy patterns of Figure 4-D preserve a consistent order of complexity index across four networks with default mode network as the most complex and central executive network as the least complex RSNs. This is also reflected using the complexity index of RSNs (the bar plot of Figure 4-F).

The same analysis with a tolerance parameter r=0.15 revealed similar ordering between the complexity distributions of RSNs, while it considerably changed the morphology of multiscale entropy curves (see Figure 4-C versus Figure 4-D – also note the difference between the y-axis limits of Figure 4-E versus Figure 4-F). The effect size analysis of the pair-wise comparisons across RSNs are summarized in the first columns of Table S3 (for r=0.5) and Table S4 (for r=0.15). According to the tables, RSNs are highly distinguishable based on their associated complexity indices at both values of r. However, an increase in r leads to a systematic decrease in the effect sizes across subjects (Hedges' g of 3.53±2.44 for r=0.5 and 2.95±2.03 for r=0.15). We also calculated power spectral density of the mean rsfMRI time series of each network. As Figure S2 suggests, the ordering of complexity indices in RSNs is independent from the signal power of their associated rsfMRI time series.

Figures 5 and 6 illustrate multiscale entropy curves of 10 RSNs using the tolerance parameters r=0.5 and r=0.15, respectively, at the downsampling rates of 2 (equivalent with a T_R of 1.44 seconds or 600 time-points) and 4 (equivalent with a T_R of 2.88 seconds or 300 time-points). We observed that the morphology of entropy values was clearly influenced by the temporal resolution of the underlying data (see the left-side panels of Figure 5 and Figure 6). This change was signified by an increase in the standard deviation and a decrease in the mean values of the complexity indices across RSNs (see the right-side panels of Figure 5 and Figure 6). In spite of that, pair-wise discrimination between the complexity index distributions of RSNs was still preserved after downsampling (see Table S3 and Table S4). However, a consistent reduction was introduced to the pair-wise Hedges' g statistics of effect size analysis in longer T_R's (from 3.53±2.44 to 2.65±1.80 and 1.49±0.93 for r=0.5 and from 2.95±2.03 to 2.01±1.29 and 1.26±0.77 for r=0.15). Figure 7 illustrates the color-coded Hedges' g measures of rsfMRI complexity index distributions using two tolerance parameter values at three temporal resolutions.

3.3 Temporal complexity of RSNs is reproducible

We performed a test-retest analysis to assess whether complexity of RSNs is reproducible across different rsfMRI scans. We computed multiscale entropy curves of 936 datasets for four rsfMRI runs of length

Entropy patterns of RSNs and their corresponding brain regions
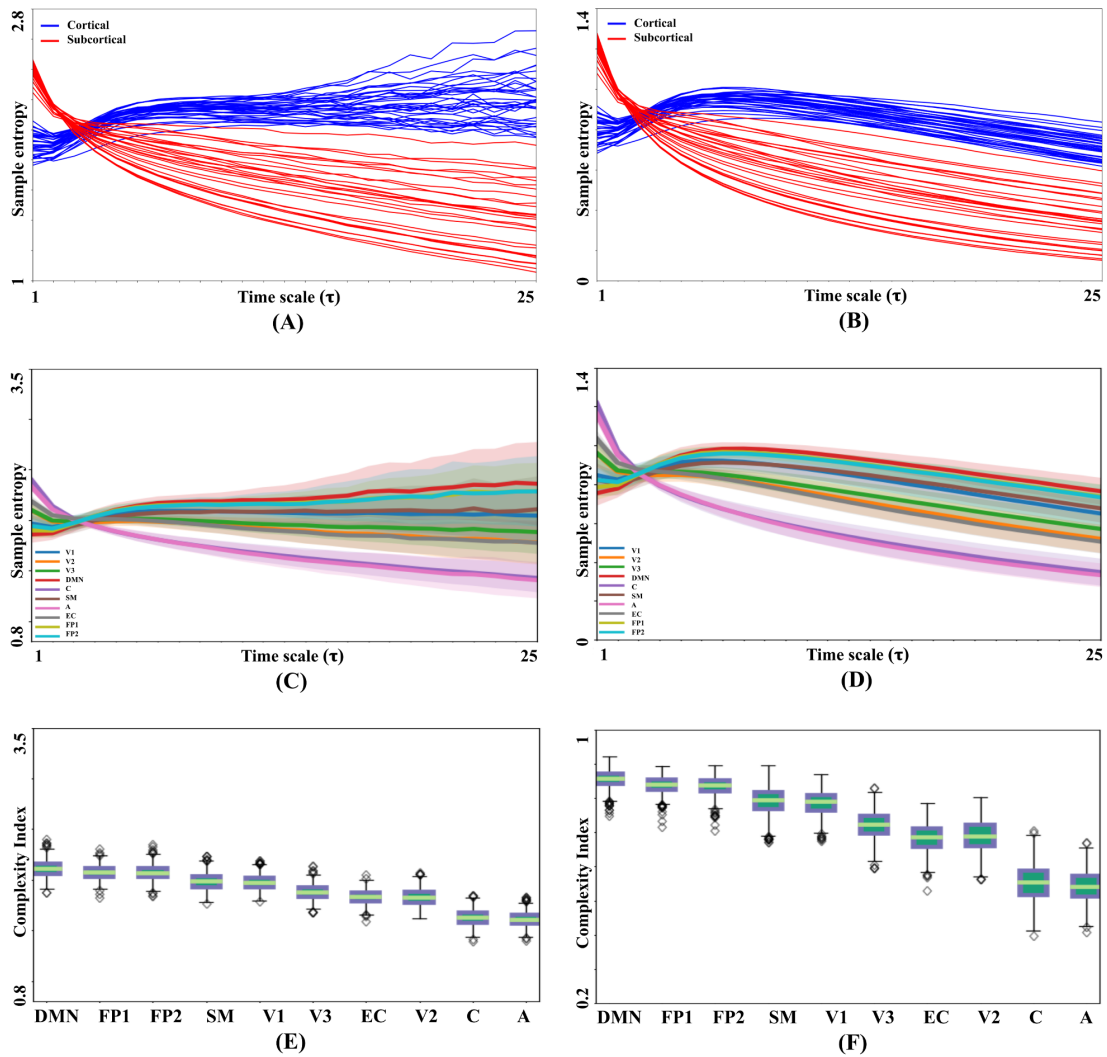
Figure 4: Multiscale entropy analysis of 936 HCP datasets. (A) and (B): Mean multiscale entropy associated with 64 brain regions covered by 10 RSNs, extracted using $r=0.15$ and $r=0.5$, respectively. (C) and (D): Shaded error bars of entropy curves for 10 RSNs using the tolerance parameters $r=0.15$ and $r=0.5$, respectively. See Figure 2 for the relation between 64 brain regions and 10 RSNs. (E) and (F): Bar plots of the complexity index values extracted from the multiscale entropy curves of (C) and (D), respectively. Each box shows the interquartile range with the median as middle horizontal line. Whiskers represent the extent of most extreme, but non-outlier data points and fliers show probable outliers. All multiscale entropy curves were obtained using the embedding dimension m of 2. **Abbreviation**: DMN = Default mode network, FP1, FP2 = Frontoparietal networks, SM = Sensorimotor network, V1, V2, V3 = Visual networks, EC = Executive control network, C = Cerebellum, A = Auditory network. See Figure S1 for the illustrations of the networks.

14.4 minutes separately (i.e., 4×1200 T_R's). We then computed the intra-class correlation coefficient of scale-dependent sample entropy values over all subjects and four sessions for the 10 RSNs and 25 time scale. Similar to the previous analyses, we repeated the test-retest analysis for two tolerance parameters, i.e., $r=0.15$ and $r=0.5$. The results are presented as color coded maps in Figure 8. As this figure shows, the tolerance parameter $r=0.5$ (used in [1]) yielded greater intra-class correlation coefficient scores than $r=0.15$. Amongst the 10 RSNs, the primary visual network had strongest test-retest reliability. The secondary visual network, default mode network and frontoparietal networks also showed good intra-class correlation coefficients. Lowest reproducibility was seen in executive control and auditory networks. For both tolerance parameters, the intra-class correlation coefficient decreased at higher scales ($\tau \geq 5$).
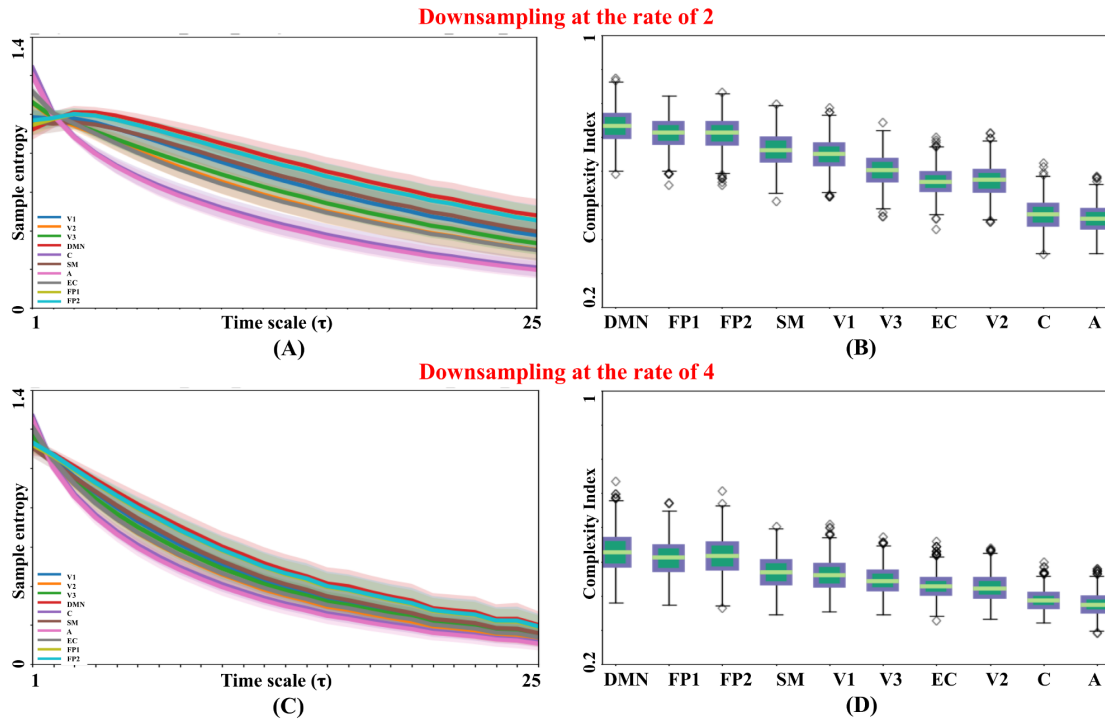
Figure 5: The effect of downsampling on the multiscale entropy curves of the HCP datasets. (A), (C): Shaded error bars of multiscale entropy curves of the HCP rsfMRI datasets after downsampling with the rates of 2 and 4, respectively. (B), (D): Bar plots of the complexity index values extracted from the multiscale entropy curves of (A) and (C), respectively. Each box shows the interquartile range with the median as middle horizontal line. Whiskers represent the extent of most extreme, but non-outlier data points and fliers show probable outliers. All multiscale entropy curves were obtained using the embedding dimension m of 2 and tolerance parameter r of 0.5. **Abbreviation**: DMN = Default mode network, FP1, FP2 = Frontoparietal networks, SM = Sensorimotor network, V1, V2, V3 = Visual networks, EC = Executive control network, C = Cerebellum, A = Auditory network. See Figure S1 for the illustrations of the networks.

3.4   Temporal complexity of RSNs correlates with higher order cognition

Amongst the five cognitive measures, fluid intelligence (Variable 4) displayed statistically significant (positive) regression coefficients (β's), in 9 out of 10 RSNs (t=3.1±0.75, df=930, p=0.023±0.052). Table S5 summarizes the multiple regression analysis results for five behavioural variables. The original complexity indices of RSNs and their predictions were correlated in all networks (Spearman correlation coefficients of 0.14±0.025, df=930, p≤0.0001). A permutation test with 10000 randomizations over subjects showed that correlation coefficients associated with all ten RSNs were above the 95th percentile of the empirical null distributions. This means that the correlation between original and predicted fMRI complexity was statistically higher than expected by chance (Figure 9). Step-wise regression analysis suggested that fluid intelligence was the only winning variable in 5 networks and one of the winning variables in 9 networks suggesting the relationship between fMRI complexity and fluid intelligence is univariate.

4   Discussion

Our study validates the hypothesis of distinct multiscale entropy signatures in functional brain networks, and reinforces the previous finding by [1]. We also build on previous research in several ways by: (i) increasing the number of subjects from 20 to 936, (ii) delineating dynamic complexity in an additional six RSNs, (iii) comparing multiple values of the tolerance parameter r for multiscale entropy analysis, (iv) investigating the effect of temporal resolution on the complexity of RSNs, (v) analysing the reproducibility of complex dynamics in functional networks over multiple recording sessions, and (vi) showing that signal complexity is related to higher order cognitive processing.

## Impact of downsampling on the complexity of RSNs ($r=0.15$)
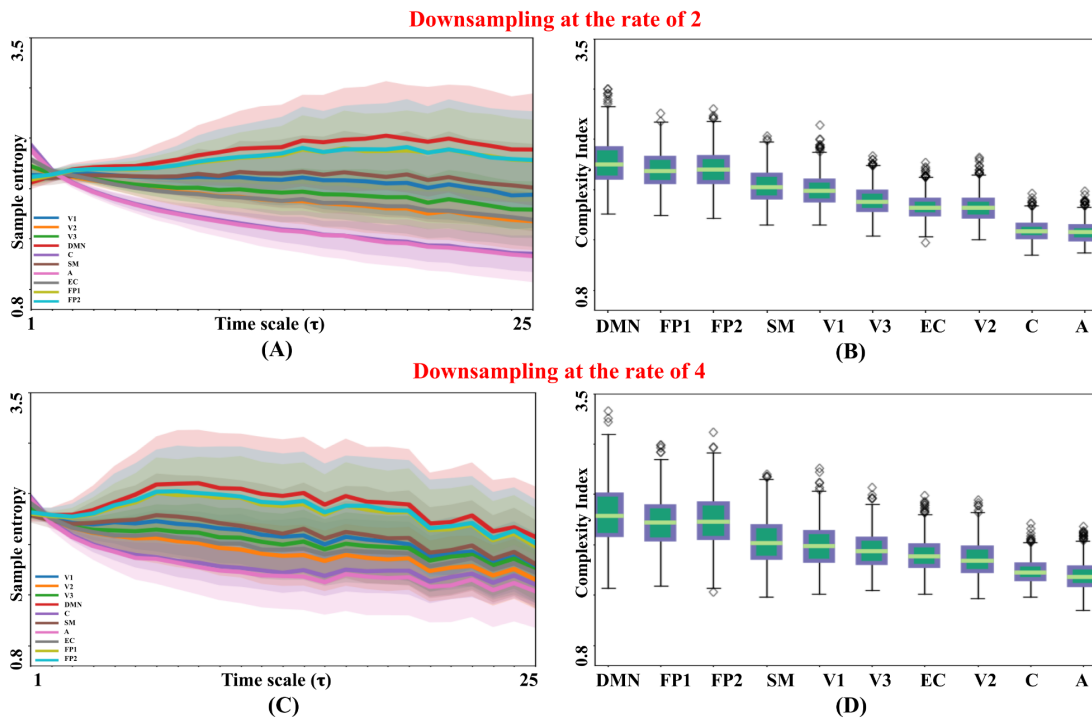
Figure 6: The labels are similar to Figure 5, except that the multiscale entropy patterns were obtained using the tolerance parameter r of 0.15. **Abbreviation**: DMN = Default mode network, FP1, FP2 = Frontoparietal networks, SM = Sensorimotor network, V1, V2, V3 = Visual networks, EC = Executive control network, C = Cerebellum, A = Auditory network. See Figure S1 for the illustrations of the networks.

The dynamics of RSNs represents a continuum from random-like behaviour within cerebellum and auditory networks, to complex behaviour within frontoparietal and default mode networks. This suggests that there is *richer* and *more integrated* information within higher order association networks compared to the primary sensory networks. In other words, their hemodynamic fluctuations present more structured patterns of information across multiple time scales. This also ties in with the findings in our linear regression analysis where network-specific fMRI complexity was related to fluid intelligence (see Table 9). This behavioural measure refers to people's ability to provide logical solutions to specific problems, in novel situations where acquired knowledge cannot be retrieved [59]. This cognitive function engages several brain networks, but the frontoparietal and executive control networks appears to be particularly important for optimal brain function (see [60] for a meta-analysis outlining important brain regions supporting in fluid intelligence). According to the Network Neuroscience Theory of Human Intelligence proposed by Aron K. Barbey [61], fluid intelligence may arise from complex interactions between multiple brain networks that drives the network dynamics responsible for adaptive higher order cognitive function. In light of this theory, is tempting to postulate that dynamic network complexity is an important component in operating, and optimizing, adaptive cognitive functions such as fluid intelligence.

Multiscale entropy patterns provide a more comprehensive picture about brain complexity than sample entropy at single time scales. In fact, single-scale sample entropy analysis could lead to misleading interpretations about the complexity of brain regions and functional networks, as demonstrated in Figure 4-A to D: the entropy values associated with cortical and sub-cortical regions may get reverse over large scales (see blue versus red curves in Figure 4-A, B, before and after $\tau=5$). The distinction in complexity between cortex and subcortex is likely related to lower temporal signal to noise ratio in rsfMRI time series within subcortical nuclei. This may be due to a higher vulnerability to thermal noise related to MRI system electronics, gradient switching artifact and physiological noise including cardiac pulsations and respiratory activity [62]. This can be further investigated using 7T data, or multi-echo data, by testing whether this distinction remains in data where the sub-cortical signal to noise ratio is improved. It is also important to note that multiscale entropy curves, and their associated complexity

Pair-wise effect size analysis of multiscale entropy patterns of RSNs
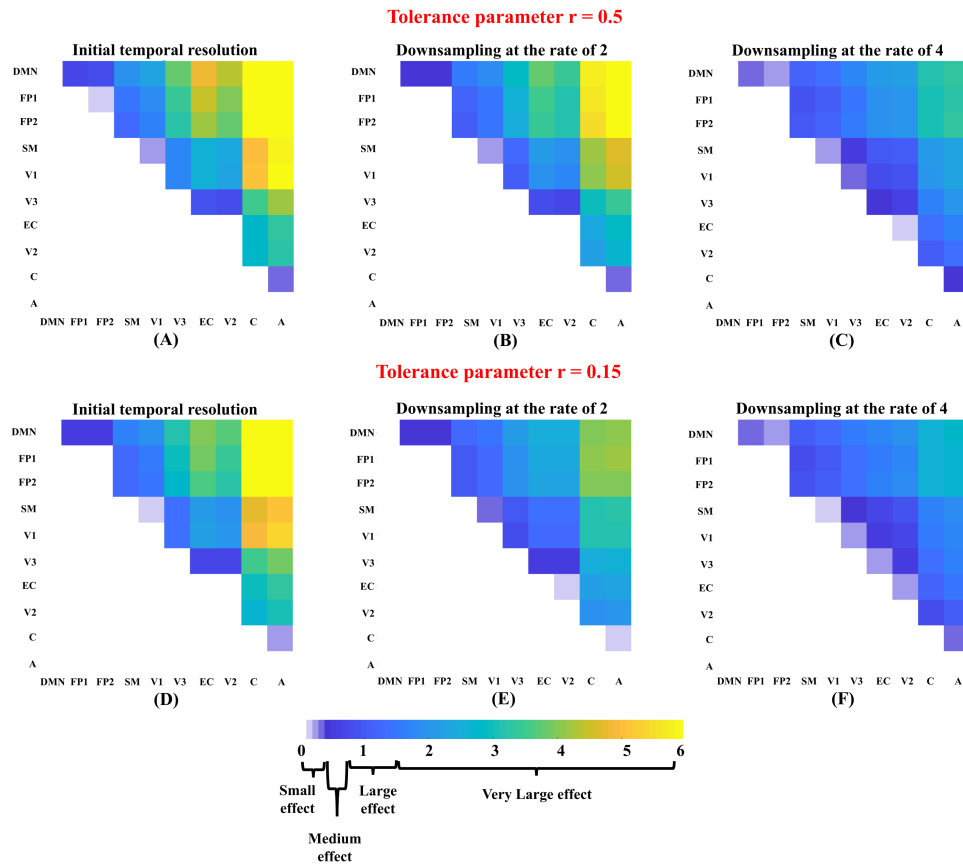
Figure 7: Hedges' g statistics obtained from effect size analysis of the complexity index distributions calculated for each pair of RSNs. The analysis has been repeated for two tolerance parameters ($r=0.15, 0.5$) and at three downsampling scenarios (no downsampling, downsampling at the rate of 2 and downsampling at the rate of 4). The Hedges' g values of less than 0.2 imply small effect, 0.2 to 0.5 are considered as medium effect, 0.5 to 1.5 are deemed as large effect and above 1.5 represent very large effect. **Abbreviation**: DMN = Default mode network, FP1, FP2 = Frontoparietal networks, SM = Sensorimotor network, V1, V2, V3 = Visual networks, EC = Executive control network, C = Cerebellum, A = Auditory network. See Figure S1 for the illustrations of the networks.

indices, are considerably affected by the choice of the tolerance parameter r, as illustrated in Figure 4, Figure 5 and Figure 6 (see [63] for another in-depth investigation of the role of the tolerance parameter r in sample entropy). However, our results suggests that the *relative network ordering* of complexity indeces is a consistent discriminative feature across RSNs. The effect size of complex signature across

Test-retest analysis over four rsfMRI runs
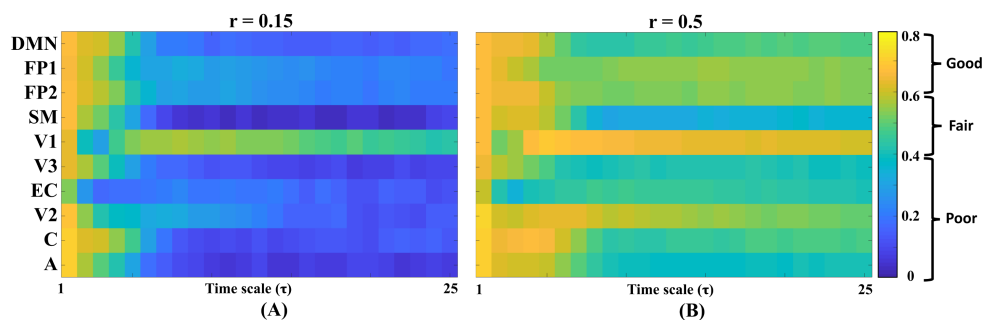
Figure 8: Test-retest analysis of the multiscale entropy curves of the HCP database over 936 subjects and four scanning sessions. The colors show the intraclass correlation coefficient values ranging from 0 to 1. The values below 0.4 show poor replicability, values between 0.4 to 0.6 show fair replicability, between 0.6 to 0.8 show good replicability and above 0.8 imply excellent reliability (do not exist in the above maps). **Abbreviation**: DMN = Default mode network, FP1, FP2 = Frontoparietal networks, SM = Sensorimotor network, V1, V2, V3 = Visual networks, EC = Executive control network, C = Cerebellum, A = Auditory network. See Figure S1 for the illustrations of the networks.

Permutation testing of the multiple regression analysis
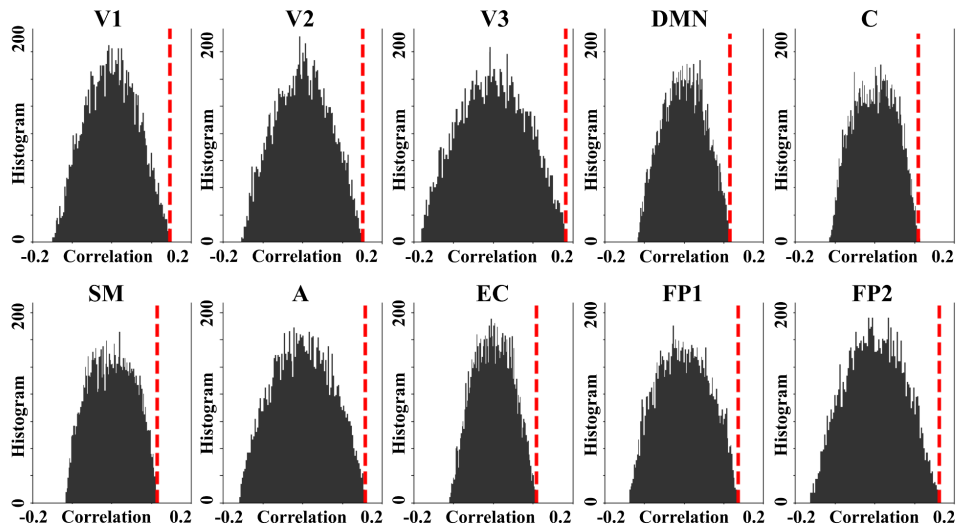
Figure 9: Empirical null distributions of the Spearman correlation coefficients obtained through a permutation testing with 10000 shuffling over subjects through multiple regression analysis between temporal complexity of RSNs (as output of the model) and five behavioural variables (as predictors). The dashed vertical line in each panel illustrates the Spearman correlation coefficient between the original complexity values (without shuffling) and their predictions. **Abbreviation**: CI = Complexity index, DMN = Default mode network, FP1, FP2 = Frontoparietal networks, SM = Sensorimotor network, V1, V2, V3 = Visual networks, EC = Executive control network, C = Cerebellum, A = Auditory network. See Figure S1 for the illustrations of the networks.

RSNs decreases at smaller r's (note the difference between the upper and lower panels of Figure 7) and at lower temporal resolutions (note the systematic reduction from right to left in Figure 7). Having said that, almost all of pair-wise Hedges' g statistics remain statistically significant after bootstrapping (see Table S3 and Table S4), also due to our large sample cohort. The embedding dimension m is another important factor in multiscale entropy analysis which controls the dimensionality of the reconstructed phase space [63]. We fixed this parameter to 2 throughout the study and it remains for future work to investigate its impact on the complexity profiles of RSNs. In addition, other rsfMRI downsampling scenarios, such as coarse-graining of time series rather than decimation, deserves more attention. The right side panels of Figure 5 and Figure 6 suggest that longer T_R's introduce more variance to complexity indices of RSNs over subjects. Therefore, the combination of a low population size and long T_R, which is a likely scenario in rsfMRI applications, may lead to unrealiable results.

Since HCP datasets consist of four rsfMRI recording sessions per subject, we were in a good position to perform a test-retest analysis of network-specidfic multiscale entropy. Figure 8 illustrates the finding in terms of two color coded maps based on the intra-class correlation coefficient, a measure of repeatability, extracted from network-specific sample entropy distributions at single time scales. As the figure suggests, sample entropy values over fine time scales ($\tau \leq 5$) are more repeatable than the values extracted at large scales. This finding was not surprising because coarse-graining step of the multiscale entropy analysis at large τ can remove original information from rsfMRI time series and reduce them into a series of random fluctuations. The primary visual network (V1 - see Figure S1) presents the most reproducible complex behaviour out of 10 RSNs. Considerably higher values of the intra-class correlation coefficient measure for $r=0.5$ in contrast to $r=0.15$ (Figure 8-B versus A) suggests that the original value of 0.5 used by McDonough and Nashiro [1] is a reasonable choice which could reveal an acceptable reliability for complex dynamic of RSNs. Focusing on the choice of $r=0.5$ (Figure 8-B), one can observe that default mode, frontoparietal and visual networks as well as the cerebellum represent the most reliable complex dynamics.

5   Conclusion

Functional brain networks represent distinctive signatures of temporal complexity which can be quantified through multiscale entropy analysis of rsfMRI. This observation is robust over a large cohort of healthy subjects, reproducible over multiple rsfMRI recording sessions, and also, it is important for optimal brain function.

Acknowledgement

Conflicts of interest

The authors declare no conflict of interest.

6 Supplementary materials

RSN templates
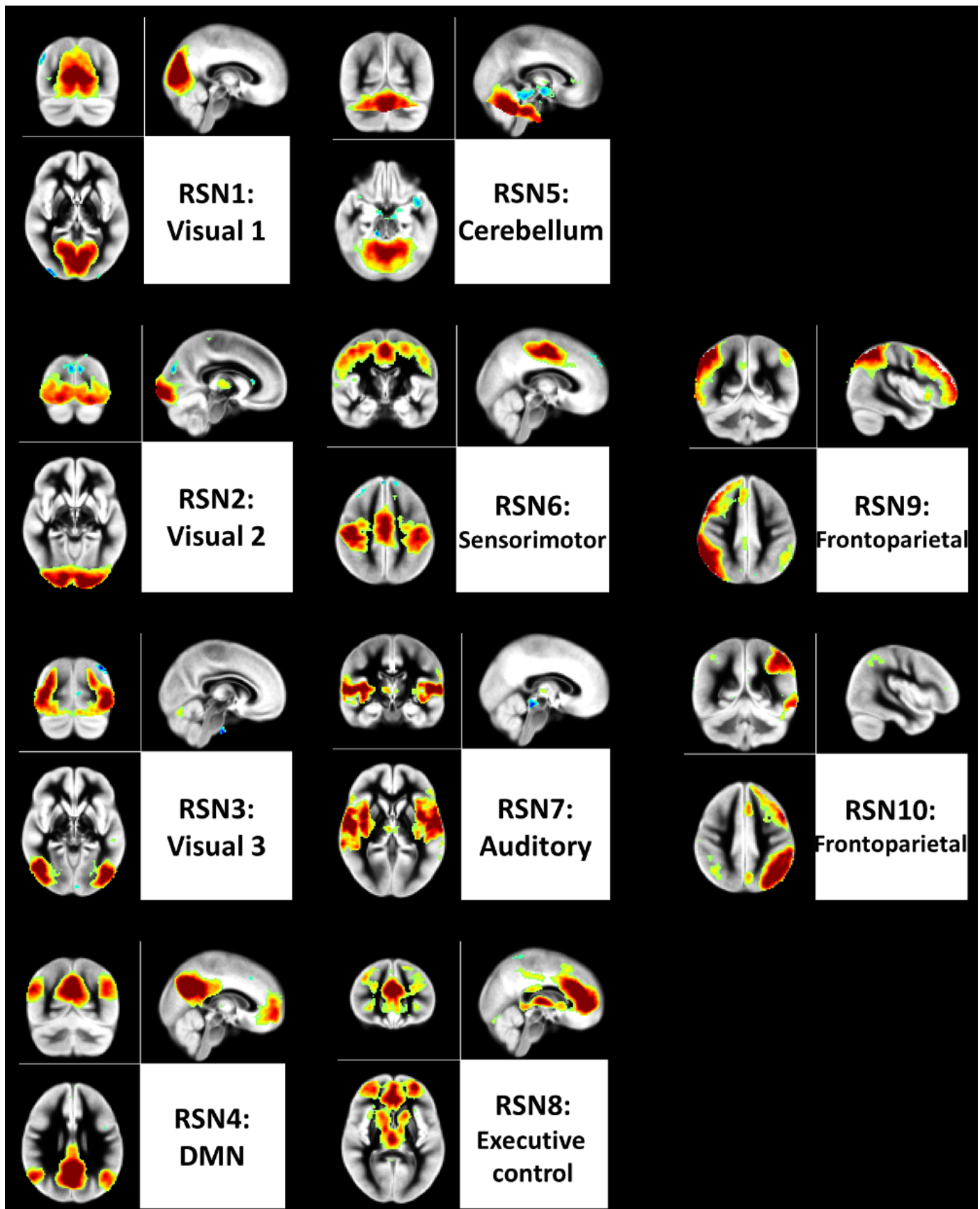
Figure S1: Spatial maps of RSNs used in this study. These maps are based on the RSNs template maps provided by Smith et al [48] and were also used in the study by MDonough and Nashiro [1].

Power spectral density analysis of RSNs
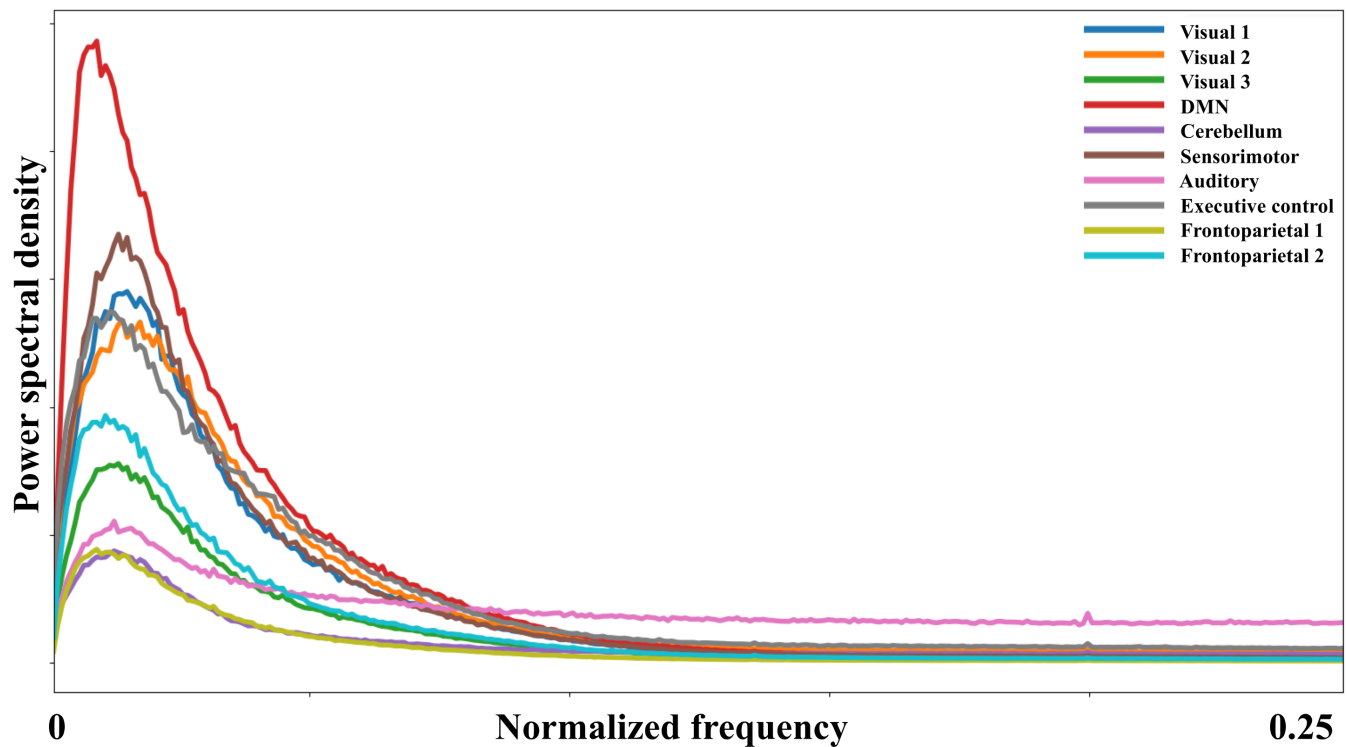
Figure S2: Mean power spectral density of 10 RSNs over 936 parcellated rsfMRI datasets. Amongst our ten RSNs, the default mode, visual and frontoparietal networks show greater entropy (Figure 4). Entropy is independent from the signal power of rsfMRI time series in our study, as there is no one-to-one relationship between power spectral density and complexity of RSNs (see Figure S2, for more information). The relative order of peak amplitudes in the frequency spectra of networks are different from the order of their complexity index distributions 4-E and Figure 4-F.

Summary of the effect size analysis results with downsampling for r=0.5

RSN pair	No DS				DS at 2				DS at 4			
	g	C1	C2	p	g	C1	C2	p	g	C1	C2	p
DMN vs FP1	0.73	0.68	0.79	0.00	0.45	0.42	0.49	0.00	0.30	0.28	0.33	0.00
DMN vs FP2	0.79	0.73	0.85	0.00	0.44	0.40	0.48	0.00	0.22	0.19	0.25	0.00
DMN vs SM	1.99	1.89	2.10	0.00	1.51	1.43	1.59	0.00	1.14	1.08	1.21	0.00
DMN vs V1	2.37	2.26	2.49	0.00	1.82	1.74	1.92	0.00	1.35	1.29	1.43	0.00
DMN vs V3	4.06	3.89	4.24	0.00	2.84	2.72	2.97	0.00	1.72	1.64	1.81	0.00
DMN vs EC	5.14	4.94	5.37	0.00	3.77	3.62	3.94	0.00	2.10	2.00	2.19	0.00
DMN vs V2	4.61	4.44	4.80	0.00	3.44	3.31	3.59	0.00	2.17	2.08	2.27	0.00
DMN vs C	7.63	7.35	7.95	0.00	5.76	5.55	5.98	0.00	3.11	2.99	3.25	0.00
DMN vs A	9.08	8.76	9.46	0.00	6.38	6.15	6.62	0.00	3.34	3.21	3.48	0.00
FP1 vs FP2	0.12	0.08	0.17	0.00	0.00	-0.03	0.03	0.91	-0.08	-0.11	-0.06	0.00
FP1 vs SM	1.49	1.41	1.58	0.00	1.14	1.07	1.21	0.00	0.89	0.83	0.95	0.00
FP1 vs V1	1.84	1.75	1.94	0.00	1.47	1.39	1.55	0.00	1.11	1.05	1.17	0.00
FP1 vs V3	3.63	3.48	3.80	0.00	2.54	2.43	2.66	0.00	1.50	1.43	1.57	0.00
FP1 vs EC	4.74	4.53	4.95	0.00	3.53	3.39	3.69	0.00	1.91	1.83	2.00	0.00
FP1 vs V2	4.22	4.05	4.41	0.00	3.18	3.06	3.31	0.00	1.99	1.90	2.08	0.00
FP1 vs C	7.33	7.04	7.65	0.00	5.64	5.44	5.86	0.00	3.03	2.91	3.17	0.00
FP1 vs A	8.78	8.44	9.15	0.00	6.32	6.09	6.56	0.00	3.28	3.15	3.42	0.00
FP2 vs SM	1.34	1.25	1.43	0.00	1.11	1.04	1.19	0.00	0.96	0.90	1.02	0.00
FP2 vs V1	1.65	1.56	1.74	0.00	1.43	1.35	1.51	0.00	1.17	1.11	1.24	0.00
FP2 vs V3	3.39	3.25	3.54	0.00	2.47	2.36	2.59	0.00	1.56	1.47	1.64	0.00
FP2 vs EC	4.46	4.28	4.66	0.00	3.43	3.28	3.58	0.00	1.96	1.87	2.05	0.00
FP2 vs V2	3.99	3.84	4.15	0.00	3.10	2.98	3.24	0.00	2.03	1.94	2.14	0.00
FP2 vs C	7.04	6.78	7.34	0.00	5.49	5.29	5.72	0.00	3.05	2.92	3.19	0.00
FP2 vs A	8.37	8.04	8.70	0.00	6.13	5.90	6.37	0.00	3.29	3.15	3.42	0.00
SM vs V1	0.17	0.12	0.22	0.00	0.26	0.22	0.31	0.00	0.19	0.15	0.24	0.00
SM vs V3	1.80	1.72	1.90	0.00	1.27	1.21	1.34	0.00	0.55	0.51	0.60	0.00
SM vs EC	2.73	2.61	2.85	0.00	2.11	2.02	2.22	0.00	0.95	0.88	1.01	0.00
SM vs V2	2.46	2.36	2.57	0.00	1.90	1.82	1.99	0.00	1.06	1.00	1.13	0.00
SM vs C	5.35	5.16	5.57	0.00	4.16	4.00	4.33	0.00	2.07	1.98	2.18	0.00
SM vs A	6.22	5.99	6.49	0.00	4.68	4.49	4.87	0.00	2.34	2.24	2.45	0.00
V1 vs V3	1.74	1.67	1.83	0.00	1.04	0.99	1.10	0.00	0.37	0.34	0.40	0.00
V1 vs EC	2.72	2.61	2.85	0.00	1.91	1.82	2.01	0.00	0.78	0.73	0.84	0.00
V1 vs V2	2.43	2.33	2.55	0.00	1.70	1.63	1.79	0.00	0.91	0.86	0.96	0.00
V1 vs C	5.44	5.24	5.69	0.00	4.04	3.88	4.21	0.00	1.97	1.88	2.06	0.00
V1 vs A	6.40	6.16	6.67	0.00	4.59	4.40	4.78	0.00	2.26	2.16	2.36	0.00
V3 vs EC	0.91	0.86	0.97	0.00	0.81	0.75	0.86	0.00	0.41	0.37	0.47	0.00
V3 vs V2	0.76	0.71	0.81	0.00	0.68	0.64	0.72	0.00	0.57	0.53	0.61	0.00
V3 vs C	3.73	3.58	3.90	0.00	2.98	2.87	3.12	0.00	1.67	1.60	1.76	0.00
V3 vs A	4.40	4.23	4.59	0.00	3.47	3.33	3.62	0.00	1.99	1.91	2.09	0.00
EC vs V2	-0.10	-0.14	-0.06	0.00	-0.07	-0.12	-0.03	0.00	0.18	0.13	0.23	0.00
EC vs C	2.93	2.81	3.06	0.00	2.35	2.25	2.46	0.00	1.32	1.25	1.39	0.00
EC vs A	3.51	3.37	3.67	0.00	2.84	2.73	2.96	0.00	1.67	1.59	1.75	0.00
V2 vs C	2.89	2.78	3.01	0.00	2.24	2.14	2.34	0.00	1.04	0.97	1.11	0.00
V2 vs A	3.42	3.28	3.57	0.00	2.66	2.55	2.78	0.00	1.37	1.29	1.44	0.00
C vs A	0.23	0.19	0.28	0.00	0.30	0.26	0.35	0.00	0.43	0.37	0.48	0.00

Figure S3: Summary of the effect size analysis of multiscale entropy results at $r=0.5$. In the table, g is the Hedges' g measure, $C1$ and $C2$ denote the lower and upper limits of the confidence interval of the Hedges' g after 2000 permutations and p represent the associated p-value.

Summary of the effect size analysis results with downsampling for r=0.15

RSN pair	No DS				DS at 2				DS at 4			
	g	C1	C2	p	g	C1	C2	p	g	C1	C2	p
DMN vs FP1	0.52	0.48	0.57	0.00	0.38	0.35	0.42	0.00	0.28	0.25	0.32	0.00
DMN vs FP2	0.51	0.46	0.57	0.00	0.34	0.30	0.38	0.00	0.21	0.17	0.24	0.00
DMN vs SM	1.68	1.58	1.78	0.00	1.27	1.20	1.35	0.00	1.05	0.99	1.12	0.00
DMN vs V1	1.89	1.80	1.99	0.00	1.54	1.46	1.62	0.00	1.24	1.18	1.31	0.00
DMN vs V3	3.15	3.02	3.28	0.00	2.19	2.10	2.29	0.00	1.52	1.44	1.60	0.00
DMN vs EC	3.99	3.83	4.16	0.00	2.63	2.53	2.75	0.00	1.76	1.68	1.85	0.00
DMN vs V2	3.66	3.53	3.82	0.00	2.60	2.50	2.71	0.00	1.91	1.82	2.01	0.00
DMN vs C	6.49	6.28	6.73	0.00	4.22	4.06	4.39	0.00	2.62	2.50	2.75	0.00
DMN vs A	6.96	6.72	7.23	0.00	4.27	4.12	4.45	0.00	2.75	2.64	2.87	0.00
FP1 vs FP2	0.02	-0.02	0.07	0.32	-0.04	-0.07	-0.01	0.02	-0.08	-0.11	-0.05	0.00
FP1 vs SM	1.31	1.23	1.40	0.00	0.97	0.91	1.04	0.00	0.83	0.77	0.88	0.00
FP1 vs V1	1.53	1.45	1.62	0.00	1.26	1.19	1.33	0.00	1.03	0.97	1.09	0.00
FP1 vs V3	2.91	2.79	3.04	0.00	1.99	1.90	2.08	0.00	1.33	1.26	1.40	0.00
FP1 vs EC	3.85	3.71	4.00	0.00	2.49	2.39	2.61	0.00	1.59	1.52	1.68	0.00
FP1 vs V2	3.47	3.32	3.62	0.00	2.45	2.35	2.56	0.00	1.76	1.68	1.85	0.00
FP1 vs C	6.57	6.35	6.82	0.00	4.34	4.18	4.52	0.00	2.57	2.46	2.69	0.00
FP1 vs A	7.12	6.86	7.40	0.00	4.39	4.23	4.56	0.00	2.70	2.59	2.82	0.00
FP2 vs SM	1.22	1.14	1.32	0.00	0.98	0.91	1.05	0.00	0.89	0.82	0.95	0.00
FP2 vs V1	1.42	1.34	1.51	0.00	1.25	1.18	1.33	0.00	1.09	1.02	1.16	0.00
FP2 vs V3	2.72	2.60	2.84	0.00	1.95	1.86	2.05	0.00	1.38	1.31	1.46	0.00
FP2 vs EC	3.59	3.44	3.74	0.00	2.42	2.32	2.54	0.00	1.64	1.56	1.73	0.00
FP2 vs V2	3.27	3.13	3.41	0.00	2.39	2.29	2.50	0.00	1.80	1.72	1.89	0.00
FP2 vs C	6.19	5.97	6.43	0.00	4.17	4.00	4.34	0.00	2.58	2.47	2.69	0.00
FP2 vs A	6.68	6.44	6.94	0.00	4.22	4.07	4.39	0.00	2.71	2.60	2.83	0.00
SM vs V1	0.11	0.05	0.16	0.00	0.25	0.20	0.30	0.00	0.18	0.13	0.22	0.00
SM vs V3	1.37	1.31	1.46	0.00	0.96	0.91	1.02	0.00	0.44	0.40	0.49	0.00
SM vs EC	2.12	2.03	2.22	0.00	1.44	1.37	1.52	0.00	0.69	0.64	0.76	0.00
SM vs V2	1.96	1.87	2.05	0.00	1.44	1.37	1.51	0.00	0.89	0.83	0.96	0.00
SM vs C	4.71	4.54	4.89	0.00	3.32	3.19	3.46	0.00	1.67	1.58	1.76	0.00
SM vs A	5.10	4.90	5.31	0.00	3.38	3.25	3.52	0.00	1.84	1.75	1.93	0.00
V1 vs V3	1.36	1.30	1.43	0.00	0.74	0.70	0.79	0.00	0.27	0.24	0.30	0.00
V1 vs EC	2.17	2.08	2.27	0.00	1.24	1.17	1.31	0.00	0.53	0.48	0.58	0.00
V1 vs V2	1.97	1.88	2.07	0.00	1.25	1.18	1.32	0.00	0.74	0.70	0.79	0.00
V1 vs C	4.91	4.73	5.11	0.00	3.26	3.12	3.41	0.00	1.58	1.50	1.66	0.00
V1 vs A	5.36	5.15	5.59	0.00	3.33	3.19	3.48	0.00	1.76	1.67	1.86	0.00
V3 vs EC	0.73	0.67	0.78	0.00	0.48	0.43	0.54	0.00	0.27	0.22	0.32	0.00
V3 vs V2	0.67	0.63	0.72	0.00	0.53	0.49	0.57	0.00	0.51	0.47	0.55	0.00
V3 vs C	3.51	3.37	3.66	0.00	2.62	2.51	2.74	0.00	1.40	1.34	1.48	0.00
V3 vs A	3.89	3.72	4.06	0.00	2.69	2.58	2.82	0.00	1.61	1.53	1.70	0.00
EC vs V2	0.01	-0.04	0.06	0.67	0.09	0.03	0.14	0.00	0.26	0.21	0.31	0.00
EC vs C	2.97	2.86	3.11	0.00	2.31	2.21	2.43	0.00	1.18	1.12	1.25	0.00
EC vs A	3.35	3.20	3.49	0.00	2.39	2.28	2.51	0.00	1.41	1.33	1.49	0.00
V2 vs C	2.70	2.59	2.82	0.00	2.02	1.93	2.12	0.00	0.83	0.77	0.90	0.00
V2 vs A	3.01	2.89	3.14	0.00	2.10	2.00	2.20	0.00	1.07	1.01	1.15	0.00
C vs A	0.21	0.16	0.26	0.00	0.12	0.07	0.17	0.00	0.35	0.29	0.41	0.00

Figure S4: Similar to Table S3, except that the results are associated with r of 0.15.

Summary of the regression analysis results between fMRI complexity and behaviour

RSN	Variable 1			Variable 2			Variable 3			Variable 4			Variable 5		
	$\beta(1)$	p	t	$\beta(2)$	p	t	$\beta(3)$	p	t	$\beta(4)$	p	t	$\beta(5)$	p	t
V1	0.03	0.41	0.82	0.01	0.73	0.35	0.07	0.07	1.82	0.05	0.17	1.37	0.05	0.15	1.44
V2	0.03	0.39	0.85	0.01	0.86	0.18	0.05	0.17	1.39	0.09	0.01	2.46	0.04	0.27	1.10
V3	0.10	0.01	2.56	0.00	0.99	-0.02	0.06	0.10	1.64	0.10	0.01	2.72	0.04	0.30	1.03
DMN	0.07	0.05	1.97	-0.03	0.48	-0.70	-0.08	0.05	-1.98	0.09	0.01	2.49	-0.05	0.19	-1.33
C	0.05	0.17	1.37	-0.04	0.27	-1.10	0.01	0.71	0.37	0.09	0.02	2.30	-0.04	0.25	-1.15
SM	0.04	0.30	1.03	-0.03	0.50	-0.67	-0.01	0.83	-0.21	0.12	0.00	3.22	-0.04	0.27	-1.11
A	0.04	0.24	1.17	-0.02	0.58	-0.55	0.03	0.48	0.71	0.16	0.00	4.40	-0.02	0.59	-0.54
EC	0.04	0.26	1.12	-0.05	0.18	-1.33	-0.03	0.40	-0.85	0.10	0.01	2.68	-0.06	0.09	-1.67
FP1	0.06	0.10	1.62	-0.03	0.46	-0.73	0.01	0.85	0.19	0.14	0.00	3.80	-0.02	0.62	-0.50
FP2	0.05	0.17	1.36	0.03	0.46	0.74	-0.02	0.63	-0.49	0.14	0.00	3.87	-0.02	0.68	-0.42

Figure S5: Summary of the multiple regression analysis results between fMRI complexity and five HCP behavioural variables including Variable 1 (*Flanker_ Unadj* or the Flanker inhibition measure), Variable 2 (*CardSort_ Unadj* or Card Sorting flexibility measure), Variable 3 (*WM_ Task_ Acc* or N-back working memory measure), Variable 4 (*PMAT24_ A_ CR* or Ravens fluid intelligence measure) and Variable 5 (*Relational_ Task_ Acc* or the relational task) [56]. **Abbreviation:** DMN = Default mode network, FP1, FP2 = Frontoparietal networks, SM = Sensorimotor network, V1, V2, V3 = Visual networks, EC = Executive control network, C = Cerebellum, A = Auditory network. See Figure S1 for the illustrations of the networks.

References

[1] I.M. McDonough and K. Nashiro. Network complexity as a measure of information processing across resting-state networks: evidence from the human connectome project. *Frontiers in Human Neuroscience*, 8:409, 2014.

[2] Hae-Jeong Park and Karl Friston. Structural and functional brain networks: From connections to cognition. *Science*, 342(6158), 2013.

[3] D.S. Bassett and E. Bullmore. Small-world brain networks. *Neuroscientist*, 12(6):512–523, Dec 2006.

[4] B. Biswal, F.Z. Yetkin, V.M. Haughton, and J.S. Hyde. Functional connectivity in the motor cortex of resting human brain using echo-planar MRI. *Magn Reson Med*, 34(4):537–541, Oct 1995.

[5] Christian F Beckmann, Marilena DeLuca, Joseph T Devlin, and Stephen M Smith. Investigations into resting-state connectivity using independent component analysis. *Philosophical Transactions of the Royal Society B: Biological Sciences*, 360(1457):1001–1013, 2005.

[6] Michael D. Fox, Abraham Z. Snyder, Justin L. Vincent, Maurizio Corbetta, David C. Van Essen, and Marcus E. Raichle. The human brain is intrinsically organized into dynamic, anticorrelated functional networks. *Proceedings of the National Academy of Sciences*, 102(27):9673–9678, 2005.

[7] William W. Seeley, Vinod Menon, Alan F. Schatzberg, Jennifer Keller, Gary H. Glover, Heather Kenna, Allan L. Reiss, and Michael D. Greicius. Dissociable Intrinsic Connectivity Networks for Salience Processing and Executive Control. *The Journal of Neuroscience*, 27(9):2349–2356, February 2007.

[8] M.P. van den Heuvel and H.E. Hulshoff Pol. Exploring the brain network: A review on resting-state fmri functional connectivity. *European Neuropsychopharmacology*, 20(8):519–534, 2010.

[9] Y. Gao, J. Zheng, Y. Li, D. Guo, M. Wang, X. Cui, and W. Ye. Abnormal default-mode network homogeneity in patients with temporal lobe epilepsy. *Medicine (Baltimore)*, 97(26):e11239, Jun 2018.

[10] C.A. Brown, Y. Jiang, C.D. Smith, and B.T. Gold. Age and Alzheimer's pathology disrupt default mode network functioning via alterations in white matter microstructure but not hyperintensities. *Cortex*, 104:58–74, Jul 2018.

[11] Vladimir L. Cherkassky, Rajesh K. Kana, Timothy A. Keller, and Marcel Adam Just. Functional connectivity in a baseline resting-state network in autism. *Neuroreport*, 17(16):1687–1690, November 2006.

[12] Michael D. Greicius, Benjamin H. Flores, Vinod Menon, Gary H. Glover, Hugh B. Solvason, Heather Kenna, Allan L. Reiss, and Alan F. Schatzberg. Resting-State Functional Connectivity in Major Depression: Abnormally Increased Contributions from Subgenual Cingulate Cortex and Thalamus. *Biological Psychiatry*, 62(5):429–437, September 2007.

[13] M. Ohta, M. Nakataki, T. Takeda, S. Numata, T. Tominaga, N. Kameoka, H. Kubo, M. Kinoshita, K. Matsuura, M. Otomo, N. Takeichi, M. Harada, and T. Ohmori. Structural equation modeling approach between salience network dysfunction, depressed mood, and subjective quality of life in schizophrenia: an ICA resting-state fMRI study. *Neuropsychiatr Dis Treat*, 14:1585–1597, 2018.

[14] Bratislav Mišić, Vasily A. Vakorin, Tomáš Paus, and Anthony R. McIntosh. Functional Embedding Predicts the Variability of Neural Activity. *Frontiers in Systems Neuroscience*, 5, November 2011.

[15] D.S. Bassett and M.S. Gazzaniga. Understanding complexity in the human brain. *Trends Cogn. Sci. (Regul. Ed.)*, 15(5):200–209, May 2011.

[16] D.S. Bassett, B.G. Nelson, B.A. Mueller, J. Camchong, and K.O. Lim. Altered resting state complexity in schizophrenia. *Neuroimage*, 59(3):2196–2207, Feb 2012.

[17] M.O. Sokunbi, V.B. Gradin, G.D. Waiter, G.G. Cameron, T.S. Ahearn, A.D. Murray, D.J. Steele, and R.T. Staff. Nonlinear complexity analysis of brain fmri signals in schizophrenia. *PLos ONE*, 9(5):1–10, 05 2014.

[18] M. Pedersen, A. Omidvarnia, J.M. Walz, A. Zalesky, and G.D. Jackson. Spontaneous brain network activity: Analysis of its temporal complexity. *Netw Neurosci*, 1(2):100–115, 2017.

[19] W.H. Thompson, P. Brantefors, and P. Fransson. From static to temporal network theory: Applications to functional brain connectivity. *Network Neuroscience*, 1(2):69–99, 2017.

[20] D.J.J. Wang, K. Jann, C. Fan, Y. Qiao, Y.F. Zang, H. Lu, and Y. Yang. Neurophysiological Basis of Multi-Scale Entropy of Brain Complexity and Its Relationship With Functional Connectivity. *Frontiers in Neuroscience*, 12:352, 2018.

[21] Danny J. J. Wang, Kay Jann, Chang Fan, Yang Qiao, Yu-Feng Zang, Hanbing Lu, and Yihong Yang. Neurophysiological Basis of Multi-Scale Entropy of Brain Complexity and Its Relationship With Functional Connectivity. *Frontiers in Neuroscience*, 12, May 2018.

[22] Xiao Liu and Jeff H. Duyn. Time-varying functional network information extracted from brief instances of spontaneous brain activity. *Proceedings of the National Academy of Sciences*, 110(11):4392–4397, 2013.

[23] Catie Chang and Gary H. Glover. Time–frequency dynamics of resting-state brain connectivity measured with fmri. *NeuroImage*, 50(1):81 – 98, 2010.

[24] Maria Giulia Preti, Thomas AW Bolton, and Dimitri Van De Ville. The dynamic functional connectome: State-of-the-art and perspectives. *NeuroImage*, 160:41 – 54, 2017. Functional Architecture of the Brain.

[25] Christopher W. Lynn and Danielle S. Bassett. The physics of brain network structure, function and control. *Nature Reviews Physics*, 1:318–332, 2018.

[26] A.L. Goldberger, D.R. Rigney, B.J. West, and A.L. Goldberger. Chaos and fractals in human physiology. *Sci. Am.*, 262(2):42–49, Feb 1990.

[27] A. L. Goldberger. Non-linear dynamics for clinicians: chaos theory, fractals, and complexity at the bedside. *Lancet (London, England)*, 347(9011):1312–1314, May 1996.

[28] James M. Shine, Michael Breakspear, Peter T. Bell, Kaylena A. Ehgoetz Martens, Richard Shine, Oluwasanmi Koyejo, Olaf Sporns, and Russell A. Poldrack. Human cognition involves the dynamic integration of neural activity and neuromodulatory systems. *Nature Neuroscience*, 22(2):289–296, 2019.

[29] Dimitri Van De Ville, Juliane Britz, and Christoph M. Michel. Eeg microstate sequences in healthy humans at rest reveal scale-free dynamics. *Proceedings of the National Academy of Sciences*, 107(42):18179–18184, 2010.

[30] Juliane Britz, Dimitri Van De Ville, and Christoph M. Michel. Bold correlates of eeg topography reveal rapid resting-state network dynamics. *NeuroImage*, 52(4):1162 – 1170, 2010.

[31] Sergi Valverde, Sebastian Ohse, Malgorzata Turalska, Bruce J. West, and Jordi Garcia-Ojalvo. Structural determinants of criticality in biological networks. *Frontiers in Physiology*, 6:127, 2015.

[32] Michael J Hawrylycz, Ed S Lein, Angela L. Guillozet-Bongaarts, Elaine H. Shen, Lydia Ng, Jeremy A. Miller, Louie N. van de Lagemaat, Kimberly Anne Smith, Amanda J. Ebbert, Zackery L. Riley, Chris Abajian, Christian F. Beckmann, Amy Bernard, Darren Bertagnolli, Andrew F. Boe, Preston M. Cartagena, M. Mallar Chakravarty, Mike Chapin, Jimmy Chong, Rachel A. Dalley, Benedict D.T. Daly, Chinh Dang, Suvro Datta, Nick Dee, Tim Dolbeare, Vance Faber, David Feng, David R. Fowler, Jeff Goldy, Benjamin W Gregor, Zeb Haradon, David R. Haynor, John George Hohmann, Steve Horvath, Robert E. Howard, A. Jeromin, Jayson M. Jochim, Marty Kinnunen, Christopher D. Lau, Evan T. Lazarz, Changkyu Lee, Tracy A. Lemon, Ling Li, Yang Li, John A Morris, Caroline C. Overly, Patrick D. Parker, Sheana E. Parry, Melissa Reding, Joshua J. Royall, Jay Schulkin, Pedro Adolfo Sequeira, Clifford R Slaughterbeck, Simón C. Smith, Andy J. Sodt, Susan M Sunkin, Beryl E. Swanson, Marquis P. Vawter, Donald S. Williams, Paul E Wohnoutka, Horst Ronald Zielke, Daniel H. Geschwind, Patrick R. Hof, Stephen M. Smith, Christof Koch, Seth G. N. Grant, and Allan R. Jones. An anatomically comprehensive atlas of the adult human brain transcriptome. *Nature*, 489:391–399, 2012.

[33] Elena A. Allen, Eswar Damaraju, Sergey M. Plis, Erik B. Erhardt, Tom Eichele, and Vince D. Calhoun. Tracking Whole-Brain Connectivity Dynamics in the Resting State. *Cerebral Cortex*, 24(3):663–676, 11 2012.

[34] Enzo Tagliazucchi, Frederic Von Wegner, Astrid Morzelewski, Verena Brodbeck, and Helmut Laufs. Dynamic bold functional connectivity in humans and its electrophysiological correlates. *Frontiers in Human Neuroscience*, 6:339, 2012.

[35] Andrew Zalesky, Alex Fornito, Luca Cocchi, Leonardo L. Gollo, and Michael Breakspear. Time-resolved resting-state brain networks. *Proceedings of the National Academy of Sciences*, 111(28):10341–10346, 2014.

[36] Amir Omidvarnia, Mangor Pedersen, Jennifer M. Walz, David N. Vaughan, David F. Abbott, and Graeme D. Jackson. Dynamic regional phase synchrony (dreps). *Human Brain Mapping*, 37(5):1970–1985, 2016.

[37] Mangor Pedersen, Amir Omidvarnia, Andrew Zalesky, and Graeme D. Jackson. On the relationship between instantaneous phase synchrony and correlation-based sliding windows for time-resolved fmri connectivity analysis. *NeuroImage*, 181:85 – 94, 2018.

[38] Raphaël Liégeois, Jingwei Li, Ru Kong, Csaba Orban, Dimitri Van De Ville, Tian Ge, Mert R Sabuncu, and B T Thomas Yeo. Resting brain dynamics at different timescales capture distinct aspects of human behavior. *Nature communications*, 10(1):2317, May 2019.

[39] Anthony Randal McIntosh, Natasa Kovacevic, and Roxane J. Itier. Increased brain signal variability accompanies lower behavioral variability in development. *PLOS Computational Biology*, 4(7):1–9, 07 2008.

[40] A.R. McIntosh, V. Vakorin, N. Kovacevic, H. Wang, A. Diaconescu, and A.B. Protzner. Spatiotemporal dependency of age-related changes in brain signal variability. *Cereb. Cortex*, 24(7):1806–1817, Jul 2014.

[41] M. Costa, A.L. Goldberger, and C.K. Peng. Multiscale entropy analysis of complex physiologic time series. *Phys. Rev. Lett.*, 89(6):068102, Aug 2002.

[42] M.D. Costa and A.L. Goldberger. Generalized multiscale entropy analysis: Application to quantifying the complex volatility of human heartbeat time series. *Entropy*, 17(3):1197–1203, 2015.

[43] J.S. Richman and J.R. Moorman. Physiological time-series analysis using approximate entropy and sample entropy. *Am. J. Physiol. Heart Circ. Physiol.*, 278(6):H2039–2049, Jun 2000.

[44] Voichiţa Maxim, Levent Şendur, Jalal Fadili, John Suckling, Rebecca Gould, Rob Howard, and Ed Bullmore. Fractional gaussian noise, functional mri and alzheimer's disease. *NeuroImage*, 25(1):141 – 158, 2005.

[45] D.C. Van Essen, K. Ugurbil, E. Auerbach, D. Barch, T.E.J. Behrens, R. Bucholz, A. Chang, L. Chen, M. Corbetta, S.W. Curtiss, S. Della Penna, D. Feinberg, M.F. Glasser, N. Harel, A.C. Heath, L. Larson-Prior, D. Marcus, G. Michalareas, S. Moeller, R. Oostenveld, S.E. Petersen, F. Prior, B.L. Schlaggar, S.M. Smith, A.Z. Snyder, J. Xu, and E. Yacoub. The human connectome project: A data acquisition perspective. *NeuroImage*, 62(4):2222 – 2231, 2012. Connectivity.

[46] Matthew F. Glasser, Stamatios N. Sotiropoulos, J. Anthony Wilson, Timothy S. Coalson, Bruce Fischl, Jesper L. Andersson, Junqian Xu, Saad Jbabdi, Matthew Webster, Jonathan R. Polimeni, David C. Van Essen, and Mark Jenkinson. The minimal preprocessing pipelines for the human connectome project. *NeuroImage*, 80:105 – 124, 2013. Mapping the Connectome.

[47] Gholamreza Salimi-Khorshidi, Gwenaëlle Douaud, Christian F. Beckmann, Matthew F. Glasser, Ludovica Griffanti, and Stephen M. Smith. Automatic denoising of functional mri data: Combining independent component analysis and hierarchical fusion of classifiers. *NeuroImage*, 90:449 – 468, 2014.

[48] Stephen M. Smith, Peter T. Fox, Karla L. Miller, David C. Glahn, P. Mickle Fox, Clare E. Mackay, Nicola Filippini, Kate E. Watkins, Roberto Toro, Angela R. Laird, and Christian F. Beckmann. Correspondence of the brain's functional architecture during activation and rest. *Proceedings of the National Academy of Sciences*, 106(31):13040–13045, August 2009.

[49] Albert C. Yang, Shih-Jen Tsai, Cheng-Hung Yang, Chung-Hsun Kuo, Tai-Jui Chen, and Chen-Jee Hong. Reduced physiologic complexity is associated with poor sleep in patients with major depression and primary insomnia. *Journal of Affective Disorders*, 131(1):179 – 185, 2011.

[50] Yan Niu, Bin Wang, Mengni Zhou, Jiayue Xue, Habib Shapour, Rui Cao, Xiaohong Cui, Jinglong Wu, and Jie Xiang. Dynamic complexity of spontaneous bold activity in alzheimer's disease and mild cognitive impairment using multiscale entropy analysis. *Frontiers in Neuroscience*, 12:677, 2018.

[51] Wen-Chin Weng, George J. A. Jiang, Chi-Feng Chang, Wen-Yu Lu, Chun-Yen Lin, Wang-Tso Lee, and Jiann-Shing Shieh. Complexity of multi-channel electroencephalogram signal analysis in childhood absence epilepsy. *PLOS ONE*, 10(8):1–14, 08 2015.

[52] Larry V. Hedges. Distribution theory for glass's estimator of effect size and related estimators. *Journal of Educational Statistics*, 6(2):107–128, 1981.

[53] Harald Hentschke and Maik C Stüttgen. Computation of measures of effect size for neuroscience data sets. *The European journal of neuroscience*, 34 12:1887–94, 2011.

[54] Duncan J. Hodkinson, Kristina Krause, Nadine Khawaja, Tara F. Renton, John P. Huggins, William Vennart, Michael A. Thacker, Mitul A. Mehta, Fernando O. Zelaya, Steven C.R. Williams, and Matthew A. Howard. Quantifying the test–retest reliability of cerebral blood flow measurements in a clinical model of on-going post-surgical pain: A study using pseudo-continuous arterial spin labelling. *NeuroImage: Clinical*, 3:301 – 310, 2013.

[55] Patrick E Shrout and Joseph L. Fleiss. Intraclass correlations: uses in assessing rater reliability. *Psychological bulletin*, 86 2:420–8, 1979.

[56] Deanna M. Barch, Gregory C. Burgess, Michael P. Harms, Steven E. Petersen, Bradley L. Schlaggar, Maurizio Corbetta, Matthew F. Glasser, Sandra Curtiss, Sachin Dixit, Cindy Feldt, Dan Nolan, Edward Bryant, Tucker Hartley, Owen Footer, James M. Bjork, Russ Poldrack, Steve

Smith, Heidi Johansen-Berg, Abraham Z. Snyder, and David C. Van Essen. Function in the human connectome: Task-fmri and individual differences in behavior. *NeuroImage*, 80:169 – 189, 2013. Mapping the Connectome.

[57] N.R. Draper and H. Smith. *Applied regression analysis, by N.R. Draper and H. Smith.* John Wiley and Sons, 1967.

[58] Madalena Costa, Ary L. Goldberger, and C.-K. Peng. Multiscale entropy analysis of biological signals. *Phys. Rev. E*, 71:021906, Feb 2005.

[59] Raymond B. Cattell. Theory of fluid and crystallized intelligence: A critical experiment. *Journal of Educational Psychology*, 54(1):1–22, 1963.

[60] Emiliano Santarnecchi, Alexandra Emmendorfer, and Alvaro Pascual-Leone. Dissecting the parieto-frontal correlates of fluid intelligence: A comprehensive ale meta-analysis study. *Intelligence*, 63:9 – 28, 2017.

[61] Aron K. Barbey. Network neuroscience theory of human intelligence. *Trends in Cognitive Sciences*, 22:8–20, 2018.

[62] Ze Wang, Yin Li, Anna Rose Childress, and John A. Detre. Brain entropy mapping using fmri. *PLOS ONE*, 9(3):1–8, 03 2014.

[63] Amir Omidvarnia, Mostefa Mesbah, Mangor Pedersen, and Graeme Jackson. Range entropy: A bridge between signal complexity and self-similarity. *Entropy*, 20(12), 2018.

[64] Lev Lafayette, Greg Sauter, Linh Vu, and Bernard Meade. Spartan performance and flexibility: An hpc-cloud chimera. Barcelona, 2016. OpenStack Summit.